# Flavor-enhanced chromomagnetic dipole moment in the bestest little Higgs framework

T. Cisneros-Pérez,[1] A. Ramirez-Morales,[2,*] R. Gamboa-Goni,[2] and C. Ortiz[1]

[1]*Unidad Académica de Física, Universidad Autónoma de Zacatecas, Solidaridad, esquina la Bufa S/N, Zacatecas 98060, Mexico*

[2]*Tecnologico de Monterrey, Escuela de Ingenieria y Ciencias, General Ramon Corona 2514, Zapopan 45138, Mexico*

(Received 10 September 2025; accepted 15 January 2026; published 12 February 2026)

We investigate the anomalous chromomagnetic dipole moment (CMDM) $\hat{\mu}_t^{\mathrm{BLHM}}$ of the top quark within the bestest little Higgs model (BLHM). Our study incorporates novel interactions arising from the extended Cabibbo-Kobayashi-Maskawa matrix in the BLHM and explores a broad region of the experimentally allowed parameter space, yielding CMDM values on the order of $10^{-3}$. This result represents an improvement over previous CMDM calculations within the BLHM and makes it competitive with other beyond the Standard Model scenarios. Experimental and model parameter uncertainties are considered and propagated through our calculations, using a Monte Carlo method.

DOI: 10.1103/zcrb-9799

## I. INTRODUCTION

The search for new physics in extensions of the Standard Model (SM) often exploits features shared by a wide class of theoretical frameworks, such as extended Higgs sectors, extra dimensions, and new symmetries that introduce additional fields. In this spirit, we take advantage of the exceptional properties of the top quark to investigate its chromomagnetic dipole moment (CMDM) within the context of the bestest little Higgs model (BLHM) [1]. The BLHM represents an advanced development within the family of little Higgs models, specifically designed to address two long-standing issues of its predecessors: custodial symmetry violation and the tension between naturalness and electroweak precision constraints. In previous little Higgs constructions, generating a Higgs quartic coupling typically induced large, phenomenologically unacceptable violations of the custodial $SU(2)_C$ symmetry, severely constrained by the $T$ parameter. In addition, a structural mass hierarchy problem emerged: Naturalness requires light top partners ($\sim$1 TeV) to stabilize the Higgs mass, whereas precision electroweak data favor significantly heavier gauge partners ($\sim$2–3 TeV). Most little Higgs models struggled to accommodate this hierarchy in a natural way.

The BLHM resolves these issues through a set of innovative theoretical features. At its core lies a modular symmetry-breaking pattern based on the coset $SO(6)_A \times SO(6)_B/SO(6)$, which naturally embeds custodial symmetry. This mechanism, realized nonlinearly through two sigma model fields, prevents the appearance of custodial-symmetry-violating divergent scalars and ensures the collective cancellation of quadratically divergent contributions to the Higgs mass at one loop. As a consequence, the new heavy gauge bosons responsible for canceling gauge-loop divergences acquire their masses at a higher decay constant $F$, while the extended quark sector—particularly the top partners—receives masses from a lower scale $f$. This built-in hierarchy ($F > f$) eliminates fine-tuning in the quark sector while allowing for naturally heavier gauge partners.

A key strength of the BLHM is its "bestest" top sector. The structure of the top Yukawa interactions is engineered to minimize the mass of the top partners for a given value of $f$, reducing fine-tuning in the Higgs sector by a factor of $\sim$9 relative to other little Higgs constructions. As a result, the model predicts a distinctive signature: exceptionally light top partners with masses in the 500–800 GeV range. This stands in sharp contrast with other beyond the Standard Model (BSM) frameworks, such as supersymmetric or composite Higgs models, where top partners are typically required to be much heavier ($>$1.5 TeV).

The phenomenological consequences of this structure are considerable. The collective symmetry-breaking mechanism, involving couplings to two nonlinear sigma fields, produces a richer phenomenology and a variety of interactions that may yield observable signals of new

*Contact author: andres.ramirez@tec.mx

*Published by the American Physical Society under the terms of the Creative Commons Attribution 4.0 International license. Further distribution of this work must maintain attribution to the author(s) and the published article's title, journal citation, and DOI. Funded by SCOAP³.*

physics across multiple sectors. Moreover, the substantial reduction in fine-tuning enables the exploration of significantly broader regions of the model's parameter space, facilitating detailed analyses of processes highly suppressed in the SM, such as flavor-changing neutral currents (FCNC) in the quark sector.

One of the most direct and quantitatively relevant consequences of the light top partners arises in the CMDM of the top quark, $\hat{\mu}_t$. Since the dominant new-physics effects contributing to this observable occur at the one-loop level, and loop amplitudes scale inversely with the mass of the particle circulating in the loop, the CMDM predicted within the BLHM is expected to be among the largest in little Higgs–type BSM models. This makes the CMDM a promising and distinctive probe for experimentally testing the BLHM.

The CMDM of the top quark has been extensively investigated in both SM and BSM contexts due to the large top-quark mass and its close connection to heavy new particles. Within the SM, several calculations [2–6] predict values of the order of $10^{-2}$. BSM contributions can also be sizable: Ref. [2] reports values of $10^{-3}$ in the type-II two-Higgs doublet model (2HDM), $10^{-2}$ in top-color-assisted technicolor (TC2), and $10^{-3}$ in 5D models. In the littlest Higgs model with T parity (LHT) [7], 2HDM scenarios yield CMDM values in the range $10^{-3} - 10^{-4}$. In the 331 model [8], the CMDM is of the order of $10^{-5}$. Effective field theory analyses [9] set an upper bound of $10^{-2}$. Models with a fourth fermion generation [10] predict values from $10^{-1}$ to $10^{-2}$. A uniparticle model examined in Ref. [11] yields values of the order of $10^{-2}$, and two-loop 2HDM calculations [12] give values between $10^{-4}$ and $10^{-3}$. Within the BLHM, the first computation of the CMDM was presented in Ref. [13], finding values in the range $10^{-5} - 10^{-6}$.

Experimentally, the CMS Collaboration has reported two independent measurements of the top CMDM using $pp$ collisions at $\sqrt{s} = 13$ TeV with an integrated luminosity of 35.9 fb$^{-1}$ [14,15]. The analysis in Ref. [14], focused on leptonic final states, yields a value in agreement with the SM. The study in Ref. [15], based on lepton + jets final states, also finds consistency with the SM but may provide enhanced sensitivity to possible deviations:

$$\hat{\mu}_t^{\mathrm{Exp}} = -0.024^{+0.013}_{-0.009}(\mathrm{stat})^{+0.016}_{-0.011}(\mathrm{syst}). \tag{1}$$

In this context, our work revisits the CMDM of the top quark within the BLHM by incorporating contributions from the new interactions introduced in Ref. [16], which include flavor-changing processes mediated by two extended mixing matrices, $V_{Hu}$ and $V_{Hd}$, analogous to the Cabibbo-Kobayashi-Maskawa (CKM) matrix [17]. We evaluate the CMDM over a broad region of the BLHM parameter space. The mixing angle $\beta$ is considered in the interval $1.10 \leq \beta \leq 1.40$, consistent with theoretical and experimental constraints [1,18–20]. Since Yukawa couplings modify the CMDM, their entire allowed range is explored. The extended symmetry couplings $g_A$ and $g_B$ are likewise varied to assess their impact. The masses of the heavy quarks in the BLHM depend on the scale $f$, while the masses of the heavy gauge bosons depend on both $f$ and $F$, with the restriction $f + F < 10$ TeV imposed by the cutoff scale $\Lambda$. Accordingly, we compute the CMDM for several viable values of $f$. Across this parameter space, we find that the CMDM reaches values of the order of $10^{-3}$, representing a substantial enhancement over previous BLHM results and potentially lying within the experimentally accessible range suggested by Eq. (1).

This paper is organized as follows. Section II provides a brief overview of the BLHM and establishes the theoretical framework of our analysis. Section III discusses the BLHM sector containing the $gt\bar{t}$ vertex relevant for the $\hat{\mu}_t^{\mathrm{BLHM}}$ calculation. In Sec. IV, we examine the allowed phase space involved in the CMDM computation, while Sec. V presents the parameter scenarios explored and outlines our methodology for error propagation. Our results are summarized in Sec. VI, including detailed figures illustrating the corresponding confidence intervals and the utility of our calculations. Finally, conclusions are presented in Sec. VII, and the Appendix lists the Feynman rules required for the CMDM computation.

## II. THEORY FRAMEWORK

To naturally include custodial $SU(2)$ symmetry, the BLHM is based on the global symmetry group $SO(6)_A \times SO(6)_B$, which is spontaneously broken to the diagonal subgroup $SO(6)_V$ at the scale $f$. This symmetry breaking occurs when the nonlinear sigma field $\Sigma$, also present in other composite Higgs and little Higgs theories, acquires a vacuum expectation value, $\langle\Sigma\rangle = 1$ [1]. As a consequence, 15 pseudo-Nambu-Goldstone bosons emerge. These consist of a zero hypercharge electroweak triplet $\phi_a$ and a triplet $\eta_a$, with $a = 1, 2, 3$, where $(\eta_1, \eta_2)$ is a complex singlet carrying hypercharge and $\eta_3$ is a real singlet. Finally, there is a real electroweak singlet scalar field $\sigma$ and two quadruplets $h_i^T = (h_{i1}, h_{i2}, h_{i3}, h_{i4})$, with $i = 1, 2$, that transform under the $SO(4)$ subgroup [16]. The $h_i$ components are the main contributors to the scalar potential, and their mixing after symmetry breaking gives rise to the scalar fields of the BLHM.

### A. Scalar, gauge, and fermion sector in the BLHM

Currently, several works in the literature extensively address each detail of the potentials that give rise to the fields of the BLHM [16,21–24]. However, in this section, we present only the elements that we consider essential for

our analysis and provide references for those we use without rewriting them.

### 1. Scalar fields

With the 15 pseudo-Nambu-Goldstone bosons, the sigma field is expressed as

$$\Sigma = e^{i\Pi/f} e^{2i\Pi_h/f} e^{i\Pi/f}, \tag{2}$$

where $\Pi$ is a $6 \times 6$ matrix that contains the fields $\phi_a$, $\eta_a$, and $\sigma$ while $\Pi_h$ comprises the quadruplets $h_i$. It is also necessary to include the nonlinear field $\Delta$, which arises from the global symmetry $SU(2)_C \times SU(2)_D$, whose breaking to the diagonal subgroup $SU(2)$ occurs at the scale $F > f$ when $\langle \Delta \rangle = 1$ [1]. From $(\Sigma, \Delta)$, one derives the scalar fields $h^0$, $A^0$, $H^{\pm}$, $H^0$, $\phi^0$, $\phi^{\pm}$, $\eta^0$, and $\eta^{\pm}$ [1,16,24]. In the BLHM, we obtain the relation $\tan\beta = v_1/v_2$, where $v^2 = v_1^2 + v_2^2 = (246\ \mathrm{GeV})^2$.

### 2. Gauge fields

The gauge terms in the BLHM are provided by the Lagrangian

$$\mathcal{L} = \frac{f^2}{8}\mathrm{Tr}(D_\mu \Sigma^\dagger D^\mu \Sigma) + \frac{F^2}{4} Tr(D_\mu \Delta^\dagger D^\mu \Delta), \tag{3}$$

where $D_\mu\Sigma$ and $D_\mu\Delta$ are covariant derivatives [1,25]. In this sector, we find the extended fields $Z'$ and $W'^{\pm}$ as well as the SM fields $Z$ and $W^{\pm}$. The group constants $g_A$ and $g_B$ are defined as

$$g = \frac{g_A g_B}{\sqrt{g_A^2 + g_B^2}}, \tag{4}$$

$$s_g = \sin\theta_g = \frac{g_A}{\sqrt{g_A^2 + g_B^2}}, \tag{5}$$

$$c_g = \cos\theta_g = \frac{g_B}{\sqrt{g_A^2 + g_B^2}}, \tag{6}$$

where $g$ is the SM $SU(2)_L$ constant and $\theta_g$ is the mixing angle.

### 3. Fermion fields

The structure of the fermion sector is given by the Lagrangian [1]

$$\begin{aligned}\mathcal{L}_t = {} & y_1 f Q^T S \Sigma S U^c + y_2 f Q_a'^T \Sigma U^c \\ & + y_3 f Q^T \Sigma U_5'^c + y_b f q_3^T (-2iT_R^3 \Sigma) U_b^c + \mathrm{H.c.},\end{aligned} \tag{7}$$

where $Q, Q'_a, q_3$ and $U^c, U'^c_5, U^c_b$ are multiplets of $SO(6)_A$ and $SO(6)_B$, respectively [25], $S = diag(1,1,1,1,-1,-1)$ is a symmetry operator, $y_1$, $y_2$, and $y_3$ are Yukawa couplings, and the terms $q_3$ and $U^c_b$, contain information about the bottom quark.

Most importantly, top-quark loops contribute the largest divergent quantum corrections to the Higgs mass in the SM; hence, the new heavy quarks in the BLHM framework play a key role in addressing the hierarchy problem. Those heavy quarks are $T$, $T^5$, $T^6$, $T^{2/3}$, $T^{5/3}$, and $B$ [1].

In the quark sector Lagrangian, the Yukawa couplings must satisfy $0 < y_i < 1$. The expression for the quark top mass contains its Yukawa coupling $y_t$ [25], such that

$$m_t^2 = y_t^2 v_1^2. \tag{8}$$

The coupling $y_t$ is related to the remaining Yukawa couplings by

$$y_t^2 = \frac{9 y_1^2 y_2^2 y_3^2}{(y_1^2 + y_2^2)(y_1^2 + y_3^2)}. \tag{9}$$

Furthermore, we can write the BLHM fine-tuning $\Psi$ in terms of the Yukawa couplings, using [25]:

$$\Psi = \frac{27 f^2}{8\pi^2 v^2 \lambda_0 \cos^2\beta} \frac{|y_1|^2 |y_2|^2 |y_3|^2}{|y_2|^2 - |y_3|^2} \log \frac{|y_1|^2 + |y_2|^2}{|y_1|^2 + |y_3|^2}, \tag{10}$$

where $\Psi$ serves as a measure to quantify how sensitive the electroweak scale is to radiative corrections in different sectors [1].

### 4. Flavor enhancement in the BLHM

The authors of Ref. [13] considered only the contributions arising from interactions between the heavy top quarks of the BLHM and the SM top quark, mediated by the bosons present in both theories. By introducing new interaction terms between the heavy top quarks and the SM light quarks and the heavy $B$ quark interactions not present in the original BLHM, we can extend the phenomenology of the model and enhance the predicted magnitude of the CMDM. To achieve this, we adopt the flavor structure presented in Refs. [16,24] for the BLHM. These structures preserve the model's fundamental symmetries and leave the coupling vertices between heavy toplike quarks and SM quarks unchanged. The modification to the BLHM in Refs. [16,24] consists of adding terms to the Lagrangians that describe interactions among the fields $(W'^{\pm}, H^{\pm}, \phi^{\pm}, \eta^{\pm})$, the heavy quark $B$, and the light SM quarks $(u, c, d, s, b)$ while avoiding tree-level flavor-changing neutral currents.

In summary, the contributions made to the BLHM in Refs. [16,24] extend the BLHM phenomenology by introducing two CKM-like unitary matrices, $V_{Hu}$ and $V_{Hd}$, into the BLHM calculations. These matrices satisfy the relation $V_{\mathrm{CKM}} = V_{Hu}^\dagger V_{Hd}$, where $V_{\mathrm{CKM}}$ is the CKM matrix [17]. We show the Feynman rules used in this work in Table V;

other rules for the flavored BLHM can be seen in Refs. [16,24].

## III. THE CHROMOMAGNETIC DIPOLE MOMENT OF THE TOP QUARK IN THE BLHM

The search for new physics can be pursued through the study of anomalous magnetic moments which arise in systems involving fermion pairs, such as electrons and muons, or in more complex composite systems, like with the neutron. The top quark's anomalous magnetic moment is a powerful probe of SM and BSM predictions. Specifically, the top-quark high mass and strong Higgs sector coupling allows for BSM virtual loop correction scenario enhancements to occur, such that if the considered process actually exists in nature, the former may fall within the scope of experimental sensitivity, thus offering indirect access to energy scales potentially inaccessible to direct detection. Moreover, the small top quark's lifetime and lack of hadronization enable the possibility to experimentally study its spin properties at high-energy particle colliders, also allowing the probing for BSM physics.

It is well known that the effective Lagrangian is nonrenormalizable for the CMDM; however, it can still parametrize sufficiently large contributions to be detectable at the LHC. Formally, the $g\bar{t}t$ vertices in Fig. 1 are used to compute one-loop corrections of the top quark's chromomagnetic dipole moment, enabling the introduction of a five-dimensional operator to parametrize the contributions to the CMDM from the BLHM. This is done via the Lagrangian

$$\mathcal{L}_{\text{eff}} = -\frac{1}{2}\bar{t}\sigma^{\mu\nu}(\hat{\mu}_t + i\hat{d}_t\gamma^5)tG^a_{\mu\nu}T^a, \tag{11}$$

where $G^a_{\mu\nu}$ is the gluon strength tensor, $T^a$ are the $SU(3)$ generators, $\hat{\mu}_t$ is the CMDM, and $\hat{d}_t$ is the chromoelectric dipole moment, such that

$$\hat{\mu}_t = \frac{m_t}{g_s}\mu_t, \qquad \hat{d}_t = \frac{m_t}{g_s}d_t. \tag{12}$$

The definitions introduced in Eq. (12) correspond to the standard expressions for the CMDM and the chromoelectric dipole moment found in the literature. Here, $m_t$ denotes the top-quark mass, and $g_s = \sqrt{4\pi\alpha_s}$ is the strong coupling constant. In our analysis, we focus exclusively on computing the chromomagnetic form factor $\mu_t$, which receives one-loop contributions from the scalar fields $S_i = (A^0, H^0, h^0, H^\pm, \phi^0, \eta^0, \sigma, \phi^\pm, \eta^\pm)$, the vector fields $V_i = (Z^0, W^\pm, \gamma, Z', W'^\pm)$, the heavy quarks $Q_j = (T, T^5, T^6, T^{2/3}, T^{5/3}, B)$, and the SM bottom quark. One novelty of this work lies in the introduction of flavor-changing interactions into the calculation of the $\widehat{\mu_t}$ within the BLHM. These flavor-changing processes are outlined in Sec. II B, and for the top quark they involve transitions from the top quark to the heavy bottom quark $B$ as well as to the SM bottom quark. The inclusion of these new contributions leads to an enhancement of the predicted value of the top-quark CMDM.

In the context of the CMDM, the valid one-loop diagrams with scalar and vector contributions are shown in Fig. 1. The amplitudes corresponding to the diagrams are given by

$$\begin{aligned}\mathcal{M}^\mu_t(S_i) = \sum_j \int \frac{d^4k}{(2\pi)^4}\bar{u}(p')(\mathcal{S}^*_i + \mathcal{P}^*_i\gamma^5)\delta_{A\alpha_1} \\ \times\left[i\frac{\not{k}+\not{p}'+m_{Q_j}}{(k+p')^2-m^2_{Q_j}}\delta_{\alpha_1\alpha_3}\right](-ig_s\gamma^\mu T^a_{\alpha_2\alpha_3}) \\ \times\left[i\frac{\not{k}+\not{p}+m_{Q_j}}{(k+p)^2-m^2_{Q_j}}\right](\mathcal{S}_i + \mathcal{P}_i\gamma^5)\delta_{B\alpha_4}V^*_{Ht}V_{Ht}u(p) \\ \times\left(\frac{i}{k^2-m^2_{S_i}}\right)\end{aligned} \tag{13}$$

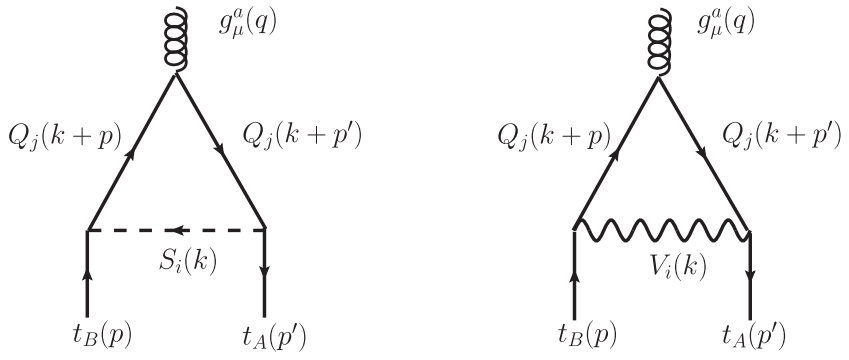



FIG. 1. The left diagram shows the interactions of the SM top quark and the BLHM heavy quarks $Q_j = (T, T^5, T^6, T^{2/3}, T^{5/3}, B)$, with the scalar fields $S_i = (A^0, H^0, h^0, H^\pm, \phi^0, \eta^0, \sigma, \phi^\pm, \eta^\pm)$. The right diagram shows the interactions of the SM top quark and $Q_j$ with the vector fields $V_i = (Z^0, W^\pm, \gamma, Z', W'^\pm)$. Both diagrams also include the SM top and bottom quarks in the loop. $q$ represents the initial gluon momentum, $k$ the loop momentum, and $p$ and $p'$ the external momentum of $t$ and $\bar{t}$, respectively. $A$ and $B$ are color indexes.

and

$$\mathcal{M}_t^{\mu}(V_i) = \sum_j \int \frac{d^4k}{(2\pi)^4}\bar{u}(p')\gamma^{a_1}(\mathcal{V}_i^* + \mathcal{A}_i^*\gamma^5)\delta_{A\alpha_1} \times \left[i\frac{\not{k}+\not{p}'+m_{Q_j}}{(k+p')^2-m_{Q_j}^2}\delta_{\alpha_1\alpha_3}\right](-ig_s\gamma^{\mu}T^a_{\alpha_2\alpha_3}) \times \left[i\frac{\not{k}+\not{p}+m_{Q_j}}{(k+p)^2-m_{Q_j}^2}\right]\gamma^{a_2}(\mathcal{V}_i+\mathcal{A}_i\gamma^5) \times \delta_{B\alpha_4}V_{Ht}^*V_{Ht}u(p) \times \left[\frac{i}{k^2-m_{V_i}^2}\left(-g_{\alpha_1\alpha_2}+\frac{k_{\alpha_1}k_{\alpha_2}}{m_{V_i}^2}\right)\right], \tag{14}$$

where $T^a_{\alpha_n\alpha_m}$ are the $SU(3)$ generators and $A$, $B$, $\alpha_n$, and $\alpha_m$ are the color indices. $q$ represents the initial gluon momentum, $k$ the loop momentum, and $p$ and $p'$ the external momentum of $t$ and $\bar{t}$, respectively. The $\mathcal{S}_i$, $\mathcal{P}_i$, $\mathcal{V}_i$, and $\mathcal{A}_i$ coefficients carry all the scalar, pseudoscalar, vector, and axial-vector contributions, respectively, from the BLHM. These coefficients are given by the vertices $\bar{Q}_jS_it$ and $\bar{t}S_i^{\dagger}Q_j$ for scalar and pseudoscalar interactions, respectively, and $\bar{Q}_jV_it$ and $\bar{t}V_i^{\dagger}Q_j$ for vector and axial interactions, respectively. The matrix elements $V_{Ht}^*V_{Ht}$ belong to the extended CKM matrix $V_{Hu}$.

Starting from the amplitudes in Eqs. (13) and (14), we compute the magnetic form factor $F_2$. Then, the BLHM correction to the top quark's CMDM is extracted from $F_2$, yielding the observable $\mu_t$, which, in turn, is substituted into the first relation in Eq. (12).

For interactions involving charged scalar and vector bosons, we consider the extended CKM matrix for the BLHM, given by $V_{\mathrm{CKM}} = V_{Hu}^{\dagger}V_{Hd}$, as introduced in Ref. [16]. Here, the unitary matrix $V_{Hu}^{\dagger}$ describes transitions from heavy quarks to light up-type quarks, while $V_{Hd}$ describes transitions from heavy quarks to light down-type quarks. This extended CKM matrix can be generalized as the product of three rotation matrices, following the formalism in Refs. [26,27]:

$$V_{Hd} = \begin{pmatrix} 1 & 0 & 0 \\ 0 & c_{23}^d & s_{23}e^{-i\delta_{23}^d} \\ 0 & -s_{23}^d e^{i\delta_{23}^d} & c_{23}^d \end{pmatrix} \times \begin{pmatrix} c_{13}^d & 0 & s_{13}^d e^{-i\delta_{13}^d} \\ 0 & 1 & 0 \\ -s_{13}e^{i\delta_{13}^d} & 0 & c_{13}^d \end{pmatrix} \times \begin{pmatrix} c_{12}^d & s_{12}^d e^{-i\delta_{12}^d} & 0 \\ -s_{12}^d e^{i\delta_{12}^d} & c_{12}^d & 0 \\ 0 & 0 & 1 \end{pmatrix}, \tag{15}$$

where the $c_{ij}^d$ and $s_{ij}^d$ entries are in terms of the flavor-mixing angles $(\theta_{12}, \theta_{23}, \theta_{13})$ and the phases $(\delta_{12}, \delta_{23}, \delta_{13})$.

## IV. PARAMETER SPACE OF THE BLHM

Schmaltz, Stolarski, and Thaler [1] considered the BLHM for a Higgs mass between 115 and 250 GeV. In subsequent BLHM publications [25,28–30], the Yukawa couplings $y_1$, $y_2$, and $y_3$ were parametrized, keeping $m_{h^0}$ at around 125 GeV. Additionally, the authors of Ref. [16] explored an alternative parameter space to optimize and constrain the BLHM in light of updated experimental data.

Experimental constraints restrict the range of $\tan\beta$ to [2, 60] [18–20]. Furthermore, due to the structure of the Yukawa sector in the BLHM, Ref. [1] imposes the condition $\tan\beta > 1$ in order to suppress one-loop radiative corrections from the top quark and heavy top partners to the Higgs mass. Additionally, the fine-tuning parameter $\Psi$ can take values in the range $0 < \Psi < 10$, with $\Psi \sim 5$ corresponding to a moderate tuning of approximately 20%. Moreover, we maintain the Yukawa couplings of the BLHM in the range $0 < y_i < 1$, ensuring that the relation in Eq. (9) is satisfied under the condition in Eq. (8). These considerations restrict the mixing angle to the range $1.1 \leq \beta \leq 1.4$ rad.

Next, we set the condition $\lambda_0 < 4\pi$ for the quartic coupling, and we use Eq. (16) [30] for determining the value of $B_\mu$:

$$B_\mu = \frac{1}{2}(\lambda_0 v^2 + m_{A^0}^2)\sin 2\beta. \tag{16}$$

The $\alpha$ mixing angle between $h^0$ and $H^0$ is determined through the relation [25]

$$\tan\alpha = \frac{1}{B_\mu - \lambda_0 v^2 \sin 2\beta}\left(B_\mu \cot 2\beta + \sqrt{\frac{B_\mu^2}{\sin^2 2\beta} - 2\lambda_0 B_\mu v^2 \sin 2\beta + \lambda_0^2 v^4 \sin^2 2\beta}\right). \tag{17}$$

The $\sigma$ boson mass is given by $m_\sigma^2 = 2\lambda_0 K_\sigma f^2$, where $K_\sigma$ is a free parameter of the BLHM [30]. For the scalar boson $\eta^0$, we use $m_{\eta^0} = m_4$, where $m_4$ is a free parameter of the model [1]; we choose $m_4 = 500$ GeV [16] due to the growing magnitudes of the masses for the new particles that have been experimentally sought. In the case of the charged scalar bosons $\phi^{\pm}$ and $\eta^{\pm}$ and the neutral scalar $\phi^0$, their masses depend not only on $m_4$, but also on both symmetry-breaking scales $f$ and $F$ as well as on one-loop contributions from the Coleman-Weinberg potential [1,28].

The BLHM is constructed to be valid up to energies of 10 TeV, as it incorporates two symmetry-breaking scales, $f$ and $F$, with the condition $f < F$. In accordance with experimental searches for heavy vector bosons, whose masses are currently investigated around 1 and

7 TeV [31], we consider the range $1 \leq f \leq 3$ TeV. Since $F$ is arbitrarily larger than $f$ but is restricted by the model to lie within $3 \leq F \leq 10$ TeV, we adopt this range to ensure that the masses of the heavy gauge bosons $Z'$ and $W'$ remain experimentally accessible with current collider capabilities.

The BLHM introduces five heavy up-type quarks and one heavy bottom-type quark. The masses of the heavy quarks depend on the Yukawa couplings $(y_1, y_2, y_3)$ and the scale $f$. For the angle $\beta$, we observe only a weak dependence, with effects below 5% for $T^5$. Furthermore, we set $m_{T^{5/3}} = m_{T^6} = m_{T^{2/3}}$ in the range 550–1650 GeV.

All of these constraints restrict the BLHM parameters to the ranges shown in Table I and Fig. 2. Table I provides a comprehensive listing of parameters and particle masses in the BLHM, constrained at different energy scales: 1, 2, and 3 TeV. Additionally, we present parameter values for the limits of the allowed $\beta$ values. One can observe that $\alpha$ and $y_3$ remain constant across energy scales, while $\Psi$, $B_\mu$, and the particle masses vary with $f$. Moreover, $\alpha$, $y_3$, $\Psi$, $B_\mu$, $m_{A^0}$, $m_{H^0}$, and $m_{H^\pm}$ exhibit significant dependence on $\beta$, whereas the remaining parameters show no such dependence.

In Fig. 2(a), the masslike parameter $B_\mu$ is plotted as a function of the mass of the neutral scalar boson $A^0$, the charged scalar $H^\pm$, and $\beta$. Larger $m_{A^0,H^\pm}$ and smaller $\beta$ yield higher $B_\mu$ values, with variations of $1.25 \times 10^5$ GeV$^2$ to $3.75 \times 10^5$ GeV$^2$. In Fig. 2(b), $B_\mu$ is plotted as a function of the mass of the scalar boson $H^0$ and $\beta$, showing a similar monotonic decrease with $\beta$ as in Fig. 2(a) but over a narrower $m_{H^0}$ range (860–940 GeV). In Fig. 2(c), the fine-tuning parameter $\Psi$ is shown as a function of $f$ and $\beta$. $\Psi$ increases with both $f$ and $\beta$, ranging from $10^{-1}$ to $10^1$, indicating regions of no tuning to moderate tuning. In Fig. 2 (d), the charged gauge mass $m_{W'}$ is plotted as a function $f$ and $F$. The mass increases predominantly with $F$ (we use $F = 5$ TeV) from ∼4 to ∼16 TeV, while the dependence on $f$ is weaker. The limits for the plots in Fig. 2 are in accordance with Table I.

Experimentally, searches for heavy neutral scalars such as $A^0$ and $H^0$ are consistent with the BLHM mass ranges. ATLAS analyzed $A \to ZH$ decays with $m_{A^0} \in [230, 800]$ GeV and $m_{H^0} \in [130, 700]$ GeV using 139 fb$^{-1}$ at $\sqrt{s} = 13$ TeV [32], while $A \to Zh$ excludes $m_{A^0} < 1$ TeV at 95% confidence level (CL) [33]. CMS results also exclude $m_{A^0} < 1$ TeV [34]. Simulated studies at the ILC with 500 fb$^{-1}$ show sensitivity to $m_{A^0} \in [200, 250]$ GeV and $m_{H^0} \in [150, 250]$ GeV [35].

Charged Higgs boson searches consider $H^\pm \to HW^\pm$ with $m_{H^\pm} \in [300, 700]$ GeV [36] and $H^+ \to t\bar{b}$ with $m_{H^+} \in [200, 2000]$ GeV [37]. For BLHM vector bosons, $W'$ masses are constrained to 2.2–4.8 TeV [38], and $Z'$ masses are excluded below 4.7 TeV [39], with other bounds in the 800–3700 GeV range [40].

TABLE I. Constrained parameters and particle masses in the bestest little Higgs model at energy scales of 1, 2, and 3 TeV. The ranges $\beta_{\min} = 1.1 \leq \beta \leq \beta_{\max} = 1.4$ rad are shown for all quantities.

| | $f$ (1 TeV) | | $f$ (2 TeV) | | $f$ (3 TeV) | | |
|---|---|---|---|---|---|---|---|
| Parameter | $\beta_{\min}$ | $\beta_{\max}$ | $\beta_{\min}$ | $\beta_{\max}$ | $\beta_{\min}$ | $\beta_{\max}$ | Unit |
| $\beta$ | 1.1 | 1.4 | 1.1 | 1.4 | 1.1 | 1.4 | Rad |
| $\alpha$ | −0.456 | −0.111 | −0.456 | −0.111 | −0.456 | −0.111 | Rad |
| $y_3$ | 0.37 | 0.32 | 0.37 | 0.32 | 0.37 | 0.32 | Rad |
| $\Psi$ | 0.102 | 0.57 | 0.41 | 2.26 | 0.92 | 5.09 | ⋯ |
| $B_\mu$ | 317189 | 155336 | 317189 | 155336 | 317189 | 155336 | GeV$^2$ |
| $m_{A^0}$ | 155.47 | 408.59 | 155.47 | 408.59 | 155.47 | 408.59 | GeV |
| $m_{H^0}$ | 876.93 | 954.87 | 876.93 | 954.87 | 876.93 | 954.87 | GeV |
| $m_{H^\pm}$ | 155.47 | 408.59 | 155.47 | 408.59 | 155.47 | 237.95 | GeV |
| $m_\sigma$ | 5010.00 | 5010.00 | 10030 | 10030 | 15040 | 15040 | GeV |
| $m_{\phi^0}$ | 4487.31 | 4487.31 | 4455.7 | 4455.7 | 4423.77 | 4423.77 | GeV |
| $m_{\phi^\pm}$ | 4490.08 | 4490.08 | 4464.3 | 4464.3 | 4437.83 | 4437.83 | GeV |
| $m_{\eta^0}$ | 500.00 | 500.00 | 500.00 | 500.00 | 500.00 | 500.00 | GeV |
| $m_{\eta^\pm}$ | 506.48 | 506.48 | 525.45 | 525.45 | 555.63 | 555.63 | GeV |
| $m_{Z'}$ | 4938.55 | 4938.55 | 5627.1 | 5627.1 | 6617.35 | 6617.35 | GeV |
| $m_{W'}$ | 4938.55 | 4938.55 | 5627.1 | 5627.1 | 6617.35 | 6617.35 | GeV |
| $m_T$ | 1063.95 | 1062.87 | 2114.13 | 2113.53 | 3167.33 | 3166.97 | GeV |
| $m_{T^5}$ | 625.36 | 599.71 | 1306.52 | 1256.88 | 1900.86 | 1978.63 | GeV |
| $m_{T^6}$ | 550.00 | 550.00 | 1100.00 | 1100.00 | 1650.00 | 1650.00 | GeV |
| $m_{T^{2/3}}$ | 550.00 | 550.00 | 1100.00 | 1100.00 | 1650.00 | 1650.00 | GeV |
| $m_{T^{5/3}}$ | 550.00 | 550.00 | 1100.00 | 1100.00 | 1650.00 | 1650.00 | GeV |
| $m_B$ | 1140.18 | 1140.18 | 2280.35 | 2280.35 | 3420.53 | 3420.53 | GeV |

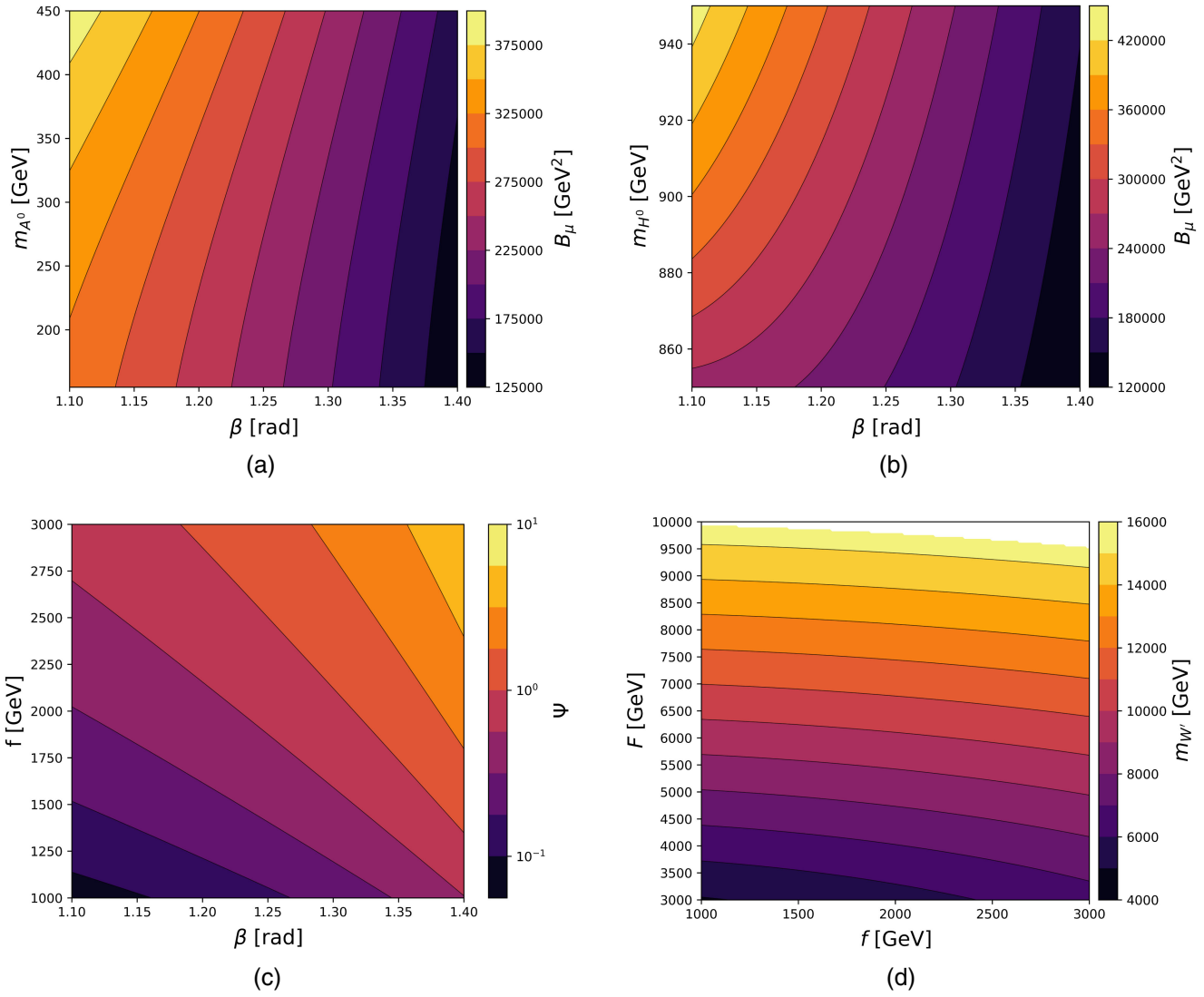



FIG. 2. Contour plots of the dependence of some selected BLHM parameters on scalar boson masses, the mixing angle $\beta$, and the symmetry-breaking scales $f$ and $F$. (a) The bilinear coupling $B_\mu$ as a function of the pseudoscalar mass $m_{A^0}$ and $\beta$. (b) $B_\mu$ as a function of the charged Higgs mass $m_{H^\pm}$ and $\beta$. (c) Fine-tuning parameter $\Psi$ as a function of $f$ and $\beta$. (d) Charged gauge mass $m_{W'}$ as a function of the two symmetry-breaking scales $f$ and $F$.

In the realm of heavy quarks, the decay $T \to Ht$ or $T \to Zt$ is analyzed in [41]. This study explores proton-proton collisions at $\sqrt{s} = 13$ TeV with an integrated luminosity of 139 fb$^{-1}$ at ATLAS, revealing no significant signals at the 95% CL for the mass of $T$ in the range of 1.6–2.3 TeV. Similar searches for $T$ and $B$ can be found in [42–44]. In [42], they also analyze the possibility of a quark with charge 5/3 like $T^{5/3}$ decaying to $Wt$, imposing a lower limit for $m_{T^{5/3}}$ of 1.42 TeV.

## V. CALCULATION OF THE CMDM

### A. Flavor-mixing scenarios

We consider six cases for the extended CKM matrices in the BLHM, for constructing the extended CKM-matrix $V_{Hd}$ [45,46].

#### 1. Case I

$V_{Hu} = \mathbf{1}$, implying $V_{Hd} = V_{\mathrm{CKM}}^\dagger$, represents a benchmark case scenario chosen to provide a basis for comparison. This choice conveys the absence of new sources of $CP$ violation beyond those already contained in the SM, thus weakly receiving contributions from the kind we will address in the cases below.

#### 2. Case II

$V_{Hd} = \mathbf{1}$, implying $V_{Hu} = V_{\mathrm{CKM}}^\dagger$, is similar to case I, as this matrix serves as a benchmark scenario where only SM sources of $CP$ violation are present; however, in this case the dominant contribution to the CMDM is expected to arise from mixing with the SM bottom quark.

### 3. Case III

$s^d_{23} = 1/\sqrt{2}$, $s^d_{12} = s^d_{13} = 0$, and $\delta^d_{12} = \delta^d_{23} = \delta^d_{13} = 0$. This choice, which departs from the standard CKM matrix, is expected to allow the inclusion of additional effects arising from mixing within the BLHM. The structure of the $V_{Hd}$ matrix implies that the first generation of the heavy quark sector does not mix, while maximal mixing is introduced between the second and third generations by setting $\theta_{23} = \pi/4$. In this scenario, all phases are set to zero in order to suppress $CP$ violation originating from BSM sources. Substituting the values of case III into the matrix $V_{Hd}$ in Eq. (15), we obtain the matrix

$$V_{Hd} = \begin{pmatrix} 1 & 0 & 0 \\ 0 & 1/\sqrt{2} & 1/\sqrt{2} \\ 0 & -1/\sqrt{2} & 1/\sqrt{2} \end{pmatrix}, \tag{18}$$

and through the product $(V^\dagger_{Hd})^{-1} V^\dagger_{\mathrm{CKM}}$, we obtain the matrix $V_{Hu}$:

$$\begin{pmatrix} 0.9737 \pm 0.0003 & 0.2210 \pm 0.0040 & 0.0080 \pm 0.0003 \\ 0.1613 \pm 0.0005 & 0.7183 \pm 0.0043 & 0.7460 \pm 0.0205 \\ -0.1559 \pm 0.0005 & -0.6606 \pm 0.0043 & 0.6873 \pm 0.0205 \end{pmatrix}, \tag{19}$$

where the uncertainties are computed analytically using the reported experimental uncertainties of the CKM matrix elements. The latter are found in Table II.

TABLE II. Masses and parameters with uncertainties used in the calculation of the $\hat{\mu}_t^{\mathrm{BLHM}}$.

| Parameter | Value |
|---|---|
| $m_Z$ | $91.1876 \pm 0.0021$ GeV |
| $m_W$ | $80.377 \pm 0.012$ GeV |
| $m_{h^0}$ | $125.11 \pm 0.11$ GeV |
| $m_t$ | $172.76 \pm 0.3$ GeV |
| $m_b$ | $4.18 \pm 0.00045$ GeV |
| $g$ | $0.6258 \pm 0.001$ |
| $g'$ | $0.3528 \pm 0.001$ |
| $\lvert V_{ud}\rvert$ | $0.97373 \pm 0.00031$ |
| $\lvert V_{us}\rvert$ | $0.2243 \pm 0.0008$ |
| $\lvert V_{ub}\rvert$ | $0.00382 \pm 0.00020$ |
| $\lvert V_{cd}\rvert$ | $0.221 \pm 0.004$ |
| $\lvert V_{cs}\rvert$ | $0.975 \pm 0.006$ |
| $\lvert V_{cb}\rvert$ | $0.0408 \pm 0.0014$ |
| $\lvert V_{td}\rvert$ | $0.0086 \pm 0.0002$ |
| $\lvert V_{ts}\rvert$ | $0.0415 \pm 0.0009$ |
| $\lvert V_{tb}\rvert$ | $1.014 \pm 0.029$ |
| $v$ | $246.22 \pm (6.06 \times 10^{-12})$ GeV |

### 4. Case IV

$s^d_{23} = 0.04183$, $s^d_{12} = 0.22501$, $s^d_{13} = 0.5$, $\delta^d_{12} = \delta^d_{23} = 0$, and $\delta^d_{13} = 1.147$. In this case, the value $s^d_{13} = 0.5$ is chosen, which is significantly larger than its SM counterpart, with the intention of enhancing mixing between the first and third generations. Additionally, $s^d_{23} = 0.04183$ corresponds to $|V_{cb}| \approx 0.041$, while $\delta^d_{13} = 1.147$ matches the CKM phase. This setup is designed to capture both SM and BSM effects within the same framework. Substituting the values of case IV into the matrix $V_{Hd}$ in Eq. (15), we obtain the matrix $V_{Hd}$:

$$\begin{pmatrix} 0.8438 & 0.1948 & 0.2056 - 0.4557i \\ -0.2331 - 0.0185i & 0.9715 - 0.0042i & 0.03622 \\ -0.1907 - 0.4436i & -0.0869 - 0.1024i & 0.8652 \end{pmatrix}, \tag{20}$$

and $V_{Hu}$:

$$\begin{pmatrix} 0.8661 \pm 0.0003 + (0.0017 \pm 0.0001)i & 0.3849 \pm 0.0036 + (0.0186 \pm 0.0006)i & 0.2233 \pm 0.0059 + (0.4622 \pm 0.0132)i \\ -0.0091 \pm 0.0007 + (0.0191 \pm 0.0001)i & 0.8972 \pm 0.0059 + (0.0083 \pm 0.0001)i & 0.0752 \pm 0.0014 + (0.0003 \pm 0.0001)i \\ -0.2019 \pm 0.0002 + (0.4550 \pm 0.0002)i & -0.0916 \pm 0.0015 + (0.1979 \pm 0.0019)i & 0.8723 \pm 0.0250 + (0.0078 \pm 0.0002)i \end{pmatrix}. \tag{21}$$

### 5. Case V

$s^d_{23} = 0.04183$, $s^d_{12} = 0.22501$, $s^d_{13} = 0.5$, and $\delta^d_{12} = \delta^d_{23} = \delta^d_{13} = 0$. Similar to case IV but with all the phases set to zero, meaning that all the $CP$ violation will come from the SM mixing. Substituting the values of case V into the matrix $V_{Hd}$ in Eq. (15), we obtain the matrix $V_{Hd}$:

$$\begin{pmatrix} 0.8438 & 0.1948 & 0.5 \\ -0.2451 & 0.9687 & 0.03622 \\ -0.4773 & -0.1531 & 0.8652 \end{pmatrix}, \tag{22}$$

and $V_{Hu}$:

$$\begin{pmatrix} 0.8672\pm0.0003 & 0.3969\pm0.0037 & 0.5222\pm0.0145 \\ -0.0213\pm0.0008 & 0.8919\pm0.0008 & 0.0750\pm0.0014 \\ -0.4958\pm0.0003 & -0.2196\pm0.0025 & 0.8677\pm0.0252 \end{pmatrix}. \tag{23}$$

#### 6. Case VI

$s_{23}^d = 0.4$, $s_{12}^d = 0.7$, $s_{13}^d = 0.5$, and $\delta_{12}^d = \delta_{23}^d = \delta_{13}^d = 0$. Similarly, setting all phases to zero implies that *CP* violation from BSM sources is not expected in this scenario. Moreover, the choice $s_{12}^d = 0.7$ corresponds to a large mixing angle compared to the Cabibbo angle. Likewise, $s_{23}^d = 0.4$ and $s_{13}^d = 0.5$ differ significantly from their SM counterparts, with the latter introducing flavor mixing that is absent in the SM. This scenario is constructed to highly depart from SM behavior and aims to capture potential effects arising from BSM physics. Substituting the values of case VI into the matrix $V_{Hd}$ in Eq. (15), we obtain the matrix $V_{Hd}$:

$$\begin{pmatrix} 0.6184 & 0.6062 & 0.5 \\ -0.7843 & 0.5144 & 0.3464 \\ -0.0472 & -0.6064 & 0.7936 \end{pmatrix}, \tag{24}$$

and $V_{Hu}$:

$$\begin{pmatrix} 0.7401\pm0.0001 & 0.7481\pm0.0045 & 0.5371\pm0.0145 \\ -0.6471\pm0.0005 & 0.3424\pm0.0044 & 0.3663\pm0.0101 \\ -0.1790\pm0.0005 & -0.5693\pm0.0038 & 0.779\pm0.0229 \end{pmatrix}. \tag{25}$$

### B. CMDM calculation and error propagation

To compute the amplitudes in Eqs. (13) and (14), we use the FeynCalc package [47] and Package X [48] for *Mathematica*. We obtain the total contribution of the BLHM to the chromomagnetic dipole by summing the scalar and vector contributions given by the amplitudes of Eqs. (13) and (14). The computation of $\hat{\mu}_t^{\rm BLHM}$ involves several measured boson and quark masses, as well as SM parameters, whose values are listed in Table II. These values are taken from the Particle Data Group [49] and include both statistical and systematic uncertainties, making it crucial to propagate them into our calculations. To achieve this, we perform a statistical simulation for error propagation: We randomly sample the experimental masses and the SM parameters from a Gaussian probability distribution, with a mean set to their central experimental value and a width equal to the squared sum of the uncertainties. We calculate $\hat{\mu}_t^{\rm BLHM}$ using sampled masses and parameters corresponding to the experimentally observed SM masses and parameters and the given values for the BLHM parameters. We repeat the procedure $10^4$ times. In this manner, we obtain a Gaussian distribution for the $\hat{\mu}_t^{\rm BLHM}$. Next, we assign the mean of the distribution as the value of the parameter and used its difference from the distribution quantiles at 68% and 95% CL, in order to extract the 68% and 95% confidence intervals (CI). The latter allows for asymmetric uncertainties. This method is known as the Monte Carlo bootstrap uncertainty propagation [50,51].

## VI. RESULTS

This section presents our results for the $\hat{\mu}_t^{\rm BLHM}$ calculations. Figures 4–6 condense the results for all the studied $\beta$ angles for cases I–VI, as described in Sec. V. Additionally, we provide individual plots for the most relevant cases and $\beta$'s considered, to show the 68% and 95% confidence interval bands arising from propagating the experimental and model parameter uncertainties. These plots are shown in Fig. 7. In Table III, we summarize the numerical values of our $\hat{\mu}_t^{\rm BLHM}$ calculations along with their uncertainty at 68% CL.

### A. Parameter analysis

In addition to the BLHM parameter space discussed in Sec. IV, we examine, given their theoretical relevance, the dependence of $\hat{\mu}_t^{\rm BLHM}$ on the gauge couplings $g_A$ and $g_B$ in Eqs. (4)–(6) and the Yukawa couplings $y_1$, $y_2$, and $y_3$, as defined in Eqs. (8) and (9). The dependence of $\hat{\mu}_t^{\rm BLHM}$ on $g_A$ and $g_B$ is shown in Fig. 3(a). Note that the variation of $\hat{\mu}_t^{\rm BLHM}$ is below 1% for most of the cases. This can be explained by the fact that $g_A$ and $g_B$ are expected to play similar roles due to their symmetric appearance in the BLHM. Figure 3(b) shows the dependence of $\hat{\mu}_t^{\rm BLHM}$ on the Yukawa couplings. In this case, the variations are more pronounced: The maximum value of the chromomagnetic moment found in this study is approximately one order of magnitude larger than the minimum value. This behavior can be attributed to the fact that the Yukawa couplings enter the calculations more directly, as they appear, for example, in all fermion masses. Along this line, we choose optimal values for the aforementioned parameters, such that the masses of the BLHM quarks and bosons are in the range of the experimental allowed values: $g_A = 2.1$, $g_B = 2.3$, $y_1 = 0.5$, and $y_2 = 0.9$. The following calculations are performed using this parameter set.

### B. Cases I–VI

Figure 4 presents the CMDM for the first case of the extended CKM matrix, with $V_{Hu} = \mathbf{1}$ and $1 < f < 3$ TeV. The figure also shows the results for the $\beta = 1.10$, 1.20, 1.30, 1.40 angles. Note that the magnitude of $\hat{\mu}_t$ remains on the order of $10^{-3}$, independently of the value of $\beta$, although a dependence is clearly observed. This behavior can also be seen in the rest of the cases, as will be shown.

TABLE III. Numerical values of the CMDM for cases I, II, V, VI and II, IV of the extended CKM matrix. In the first column the $\beta$ angles are indicated. The second, third, and fourth columns contain the computed CMDM values for $f = 1$, 2, 3 TeV, respectively. The uncertainties are reported at 68% CL.

| | Case I, II, V, VI | | |
|---|---|---|---|
| $\beta$ [rad] | $f = 1$ TeV | $f = 2$ TeV | $f = 3$ TeV |
| 1.1 | $(-6.47^{+0.06}_{-0.06}) \times 10^{-3}$ | $(-6.55^{+0.05}_{-0.05}) \times 10^{-3}$ | $(-6.71^{+0.05}_{-0.05}) \times 10^{-3}$ |
| 1.2 | $(-6.13^{+0.06}_{-0.06}) \times 10^{-3}$ | $(-6.37^{+0.05}_{-0.05}) \times 10^{-3}$ | $(-6.56^{+0.05}_{-0.05}) \times 10^{-3}$ |
| 1.3 | $(-5.99^{+0.06}_{-0.06}) \times 10^{-3}$ | $(-6.31^{+0.05}_{-0.05}) \times 10^{-3}$ | $(-6.53^{+0.05}_{-0.05}) \times 10^{-3}$ |
| 1.4 | $(-6.0^{+0.06}_{-0.06}) \times 10^{-3}$ | $(-6.36^{+0.05}_{-0.05}) \times 10^{-3}$ | $(-6.58^{+0.05}_{-0.05}) \times 10^{-3}$ |
| | Case II, IV | | |
| $\beta$ [rad] | $f = 1$ TeV | $f = 2$ TeV | $f = 3$ TeV |
| 1.1 | $(-6.46^{+0.06}_{-0.06}) \times 10^{-3}$ | $(-6.55^{+0.05}_{-0.05}) \times 10^{-3}$ | $(-6.7^{+0.05}_{-0.05}) \times 10^{-3}$ |
| 1.2 | $(-6.13^{+0.06}_{-0.06}) \times 10^{-3}$ | $(-6.37^{+0.05}_{-0.05}) \times 10^{-3}$ | $(-6.57^{+0.05}_{-0.05}) \times 10^{-3}$ |
| 1.3 | $(-5.99^{+0.06}_{-0.06}) \times 10^{-3}$ | $(-6.31^{+0.05}_{-0.05}) \times 10^{-3}$ | $(-6.53^{+0.05}_{-0.05}) \times 10^{-3}$ |
| 1.4 | $(-5.99^{+0.06}_{-0.06}) \times 10^{-3}$ | $(-6.35^{+0.05}_{-0.05}) \times 10^{-3}$ | $(-6.58^{+0.05}_{-0.05}) \times 10^{-3}$ |

In Fig. 5, we plot all six cases for $\beta = 1.10$ rad. We note the formation of two groups, one with two curves, while the other with four nearly overlapping curves, corresponding from top to bottom, to cases II and IV and cases I, III, V, and VI, respectively. This allows us to treat our CMDM results as though only two cases effectively exist, namely, case II, IV and case I, III, V, VI. Profiting from this, Fig. 6 plots all cases for all $\beta$'s, where the solid lines represent case I, III, V, VI, while the dashed ones represent case II, IV. Notice that the plot encompasses all I–VI studied cases, via displaying four pairs of curves, the blue, green, black, and red ones, corresponding from top to bottom to the $\beta = 1.30$, 1.40, 1.20, and 1.10 rad angles, respectively. Furthermore, note that the case splitting behavior seen in Fig. 5 for the $\beta$ value of 1.10 now holds for the rest of the $\beta$ values but in a minor degree—practically vanishing for $\beta = 1.20$. Although we expected to observe a stronger separation between the six different scenarios, the similarity can be attributed to the fact that, in this work, we consider only flavor-changing interactions between the SM top quark and the SM bottom quark, as well as the BLHM heavy $B$ quark. As seen in Eqs. (19)–(25), the matrix elements, which encode the information of these flavor-changing processes, are quite close to each other. Despite the fact that the difference between them can be as large as 30%, this does not significantly propagate through the final calculation of the top quark's CMDM. This result opens the opportunity to explore the possibility of mixing with other quark generations in future investigations, where the elements of different extended matrices may have a greater

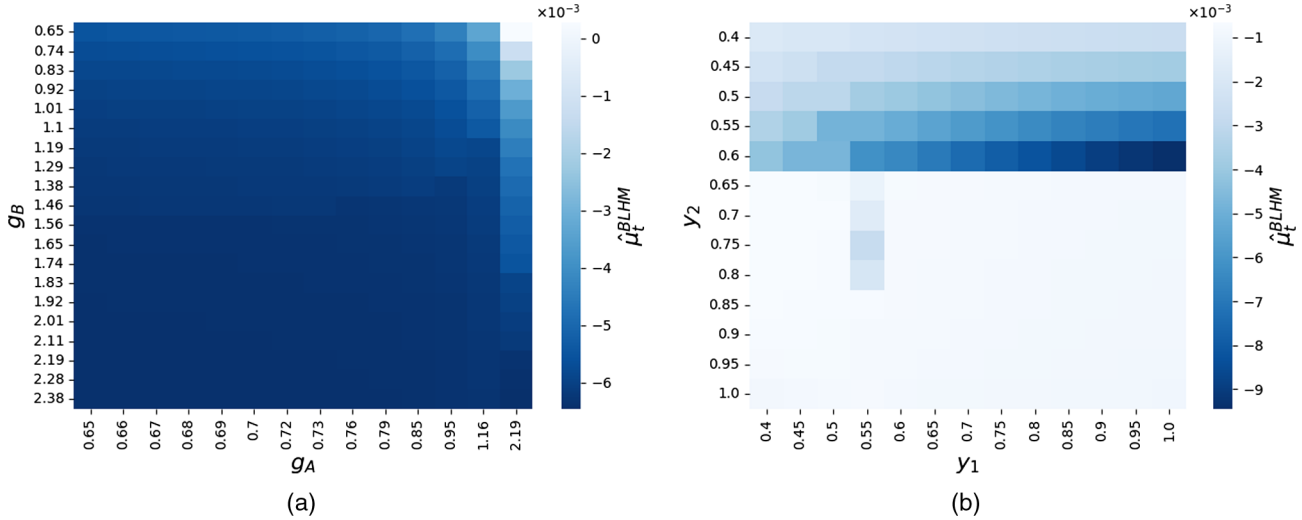



FIG. 3. (a) Dependence of $\hat{\mu}_t^{\mathrm{BLHM}}$ on the parameters $g_A$ and $g_B$. (b) CMDM dependence on the ratio between $y_1$ and $y_2$.

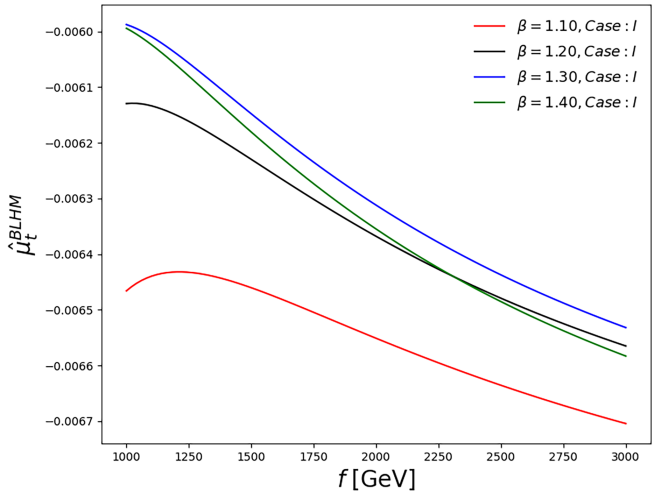



FIG. 4. Case I. Total contributions to the CMDMs with the CKM matrix $V_{Hu} = \mathbf{1}$ and four different $\beta$ angles.

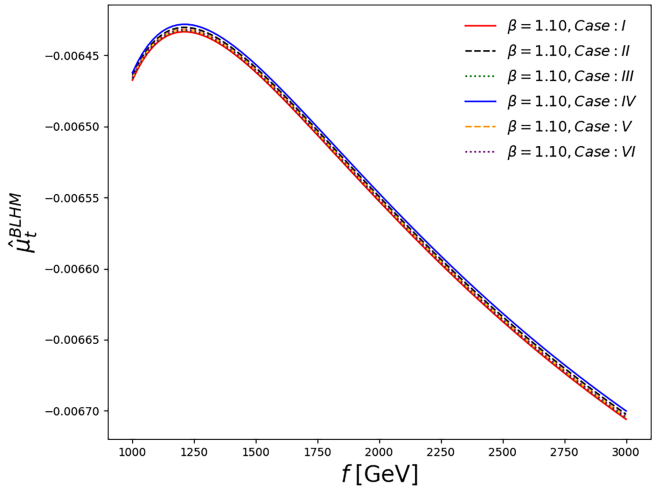



FIG. 5. Cases I–VI. Total contributions to the CMDMs with the full spectrum of possible CKM matrix ($V_{Hu}$) values, for a $\beta$ value of 1.10 rad.

impact. In order to visualize the impact of experimental uncertainties for our effective groups, we present individual plots of the $\hat{\mu}_t^{\mathrm{BLHM}}$ for each of them, for the different $\beta$ angles. These plots are intended to ease the display of the confidence intervals in our calculations, due to error propagation. Figure 7 shows the $\hat{\mu}_t^{\mathrm{BLHM}}$ for cases I, III, V, VI (upper plots) and II, IV (lower plots), as discussed in Sec. VI B. Note that, in both effective cases, the error bands resulting from experimental uncertainties yield values on the order of $10^{-3}$. This indicates that our calculations are stable and consistent. Moreover, the main variations in the central values of our calculations for $\hat{\mu}_t^{\mathrm{BLHM}}$ arise primarily from the variation of the model parameters: $\beta$, $y_1$, $y_2$, $y_3$, and $f$. Thus, these error bands may help determine whether a deviation in the measured CMDM is truly a prediction of the model or merely a consequence of experimental uncertainties.

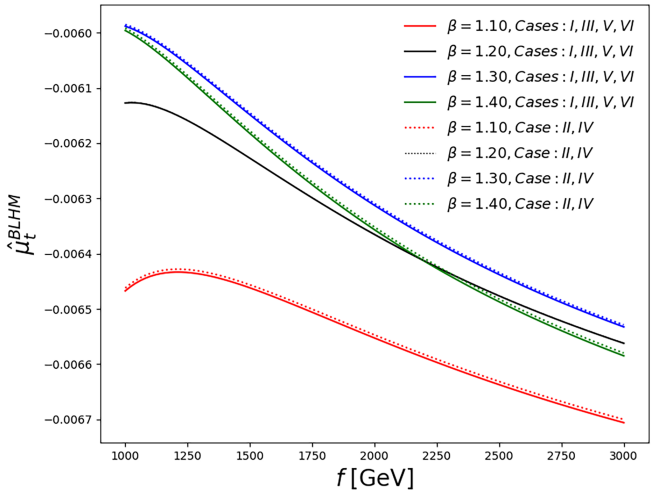



FIG. 6. Cases I–VI. Total contributions to the CMDMs with the full spectrum of possible CKM matrix ($V_{Hu}$) and $\beta$ values. The solid lines represent case I, III, V, VI, while the dashed ones represent case II, IV.

Finally, Table III displays our numerical values for the CMDM according to $f = 1$, 3 TeV. As suggested by our plots, these values are nearly identical across all six cases.

### C. Comparison with other works

Table IV presents a comparison of the absolute value of the top-quark chromomagnetic dipole moment $|\hat{\mu}_t|$ for SM and BSM calculations, as reported in various references. The SM predictions (upper block) consistently yield values of the order of $10^{-2}$. In contrast, BSM models (lower block) exhibit a broader range of predictions: Values between $10^{-3}$ and $10^{-2}$ are obtained in the 2HDM-II, technicolor TC2, and 4GTHDM frameworks, while significantly smaller values, down to $10^{-6}$, are predicted in the $Z'$ FCNC. Our result, obtained within the flavor-enhanced BLHM framework, is labeled in the table as "this work" and gives $|\hat{\mu}_t| \sim 10^{-3}$. The wide range of predictions highlights the sensitivity of $\hat{\mu}_t$ to new-physics effects, particularly those involving extended scalar, gauge, or fermionic sectors that directly impact the top-quark interactions.

These BSM contributions are expected to modify the SM values; hence, any experimentally measured deviation of the CMDM with respect to the SM calculations might serve as an indication of BSM physics. The current CMDM experimental sensitivity achieved at the LHC is of the order $10^{-3}$; therefore, enhancing upon the latest BLHM CMDM predictions, all lying below $10^{-4}$, constitutes a relevant improvement. Furthermore, when comparing our results with other BSM predictions, we find that the inclusion of flavor mixing in the BLHM framework makes our calculation competitive with results obtained in other BSM scenarios.

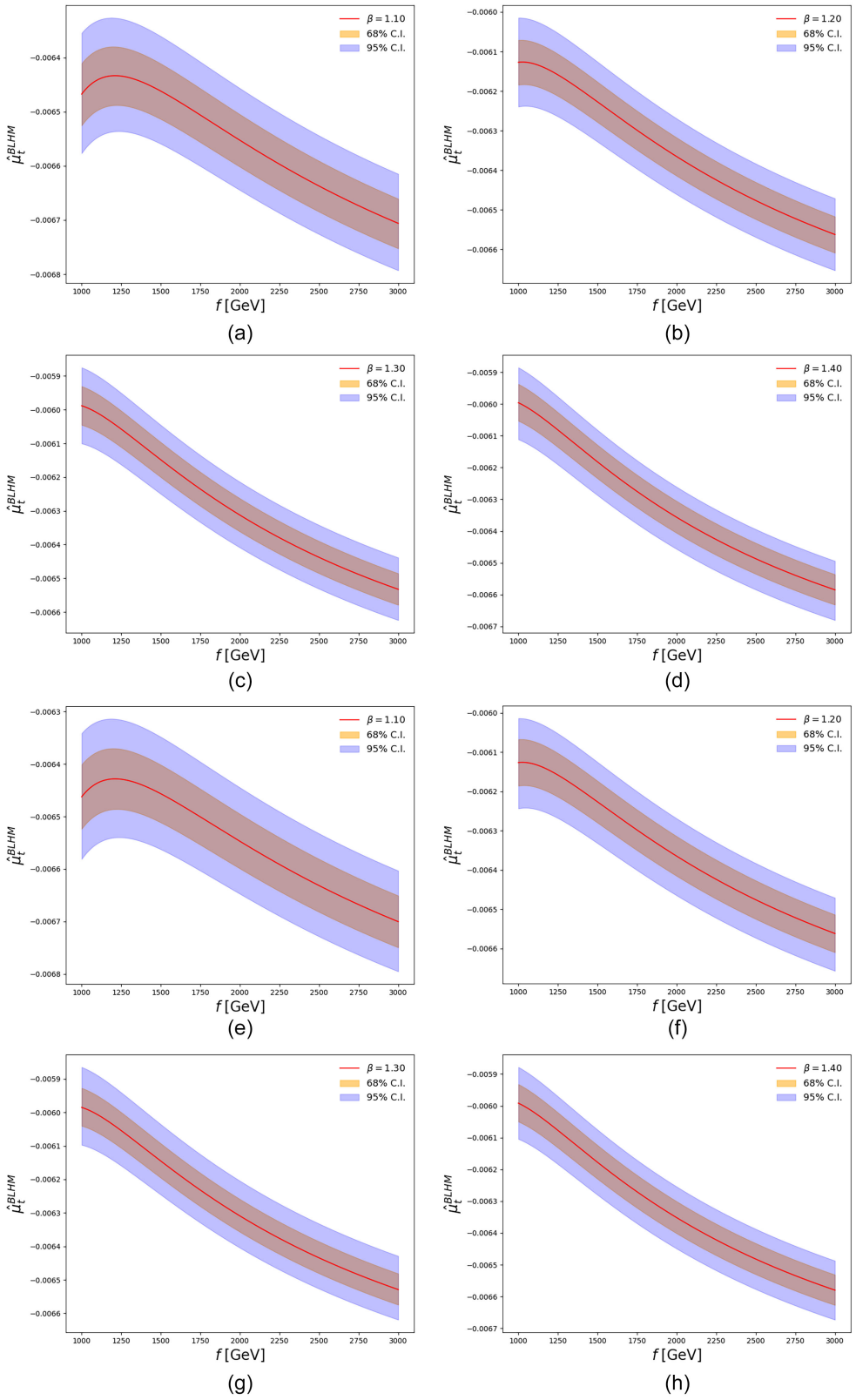



FIG. 7. Cases I, III, V, VI and II, IV. Total contributions to the CMDM for $\beta$ angle indicated in each plot. Plots (a)–(d) refer to case I, III, V, VI, while (e)–(h) plots are for case II, IV. The solid red lines correspond to the central values of our calculations. The orange and blue bands are the 68% and 95% CI, respectively, which arise from the uncertainty propagation described in Sec. V.

TABLE IV. Comparison of the absolute value of the top-quark chromomagnetic dipole moment $|\hat{\mu}_t|$ reported in various studies. SM predictions are displayed in the upper block. BSM predictions are displayed in the lower block. This work's result, for the flavor-enhanced BLHM $|\hat{\mu}_t|$, is found and highlighted in the lower block.

| Model | $\lvert\hat{\mu}_t\rvert$ |
|---|---|
| SM | $10^{-2}$ [4] |
| SM | $10^{-2}$ [2] |
| SM | $10^{-2}$ [3] |
| SM | $10^{-2}$ [6] |
| Enhanced BLHM | $10^{-3}$ *[this work]* |
| BLHM | $10^{-6} - 10^{-5}$ [13] |
| 2HDM-II | $10^{-3}$ [2] |
| Technicolor TC2 | $10^{-2}$ [2] |
| Extra dimensions 5D | $10^{-3}$ [2] |
| LH T parity | $10^{-3} - 10^{-4}$ [7] |
| 331 | $10^{-5}$ [8,2] |
| $Z'$ FCNC | $10^{-6}$ [5] |
| Decoupling EFT | $< 10^{-2}$ [9] |
| 4GTHDM | $10^{-2} - 10^{-1}$ [10] |
| Uniparticle | $10^{-2}$ [11] |
| Two-loop 2HDM | $10^{-4} - 10^{-3}$ [12] |

In particular, comparing our work with Ref. [13], we note that one of the most important differences between this work and Ref. [13] is that the authors of Ref. [13] did not include interactions involving the $W$ boson and the SM $b$-quark fields. In contrast, the inclusion of the $b$ quark through flavor mixing is a key feature of the present analysis. By neglecting these interactions, Ref. [13] misses a significant portion of the phenomenology that contributes directly to $\hat{\mu}_t$. The inclusion of the $W$ boson and the fermion flavor structure enhances these contributions, leading to the nearly 2-orders-of-magnitude increase observed in our results. Consequently, the sizable discrepancy between Ref. [13] and this work can be attributed to the inclusion of these effects in our study.

Another difference between this work and Ref. [13] is that several important constants, namely $g_A$, $g_B$, and the Yukawa couplings $y_i$, are fixed to single values in Ref. [13]. In contrast, we perform a parameter scan aimed at enhancing $\hat{\mu}_t$, which is treated as a primary objective of this work. Accordingly, the free parameters, subject to physical constraints, are chosen so as to maximize $\hat{\mu}_t$, as shown in Fig. 3.

### D. Utility of the calculations

Precision theoretical calculations of anomalies for the top-quark CMDM provide a clear motivation for experimentalists to update and refine these measurements. Such calculations indicate the level of precision required to potentially observe new-physics effects and test models like the BLHM, thus motivating improved analyses using existing data, advanced techniques, and future experimental configurations, such as the HL-LHC and prospective lepton colliders.

While current extractions of the $\hat{\mu}_t$ are limited by systematic uncertainties at the $\sim 10^{-2}$ level [52], several leading contributions are expected to improve in the HL-LHC era. Pileup effects can be mitigated with modern algorithms such as PUPPI and machine-learning-based approaches [53,54]. Jet flavor tagging is expected to benefit from state-of-the-art deep learning taggers [55–57], with demonstrated gains in CMS studies [58], and from the phase-II minimum ionizing particle timing detector enabling improved performance under extreme pileup [59]. Trigger-related uncertainties should decrease with much larger data samples at the HL-LHC [60] and with the development of real-time machine learning for electron identification in trigger hardware [61]. Jet energy scale and resolution uncertainties are also expected to improve through detector upgrades that enhance particle-flow reconstruction [62] and through deep-learning-based calibrations for large-radius jets (improving both scale and resolution at high $p_{\mathrm{T}}$) [63]. Additional reductions are anticipated from improved top-quark $p_{\mathrm{T}}$ reweighting using machine learning [64], continued progress on parton distribution functions and $\alpha_s$ determinations [65–67], and more precise luminosity measurements [68]. Moreover, systematic effects from parton-shower radiation, matching scales, and the underlying event are the subject of dedicated recent studies [69,70], and $b$-quark fragmentation uncertainties are expected to decrease for HL-LHC $b$-tagging performance [71]. Together with the large increase in integrated luminosity foreseen for the HL-LHC [60], these developments motivate continued CMDM studies even if ultimate sensitivity to the $\sim 10^{-3}$ regime may require future collider facilities.

Future lepton colliders, envisioned as high-precision facilities capable of indirectly probing BSM physics through precision measurements, will allow for the anomalous CMDM of the top quark to be constrained using angular distributions in $t\bar{t}$ production [52]. Proposed facilities such as CLIC, ILC, and FCC-ee plan to operate at center-of-mass energies near the $t\bar{t}$ production threshold with integrated luminosities ranging from several hundred to several thousand $\mathrm{fb}^{-1}$ [72–76], while a future top-quark program at CEPC is under consideration [77–82]. The clean experimental environment of $e^+e^-$ collisions enables a substantial reduction of systematic uncertainties relative to hadron colliders, including negligible pileup, excellent jet energy resolution, highly efficient flavor tagging, triggerless or near-unity trigger efficiency, and the absence of parton distribution function and underlying-event effects [73,83–91]. Additional improvements are expected from advances in parton-shower matching [92], luminosity determination [93], and heavy-flavor fragmentation measurements [94–97]. Combined with favorable

statistical scaling due to high efficiency and purity, these features position future lepton colliders to achieve unprecedented, potentially subpercent, sensitivity to top-quark CMDM effects, establishing them as powerful precision probes of new physics.

Moreover, the CLICdp Collaboration [98] performed an analysis of semileptonically decaying top quarks at the three energy stages of CLIC reporting statistical uncertainties for the $t\bar{t}$ cross section $\sigma_{t\bar{t}}$, and the forward-backward asymmetry $A_{FB}$, of less than 5%. Although they did not perform a thorough analysis for the systematic uncertainties, they discussed *ad hoc* variations to conservatively assess the impact of the largest systematics associated with the analysis of radiative events, reporting values below 5% for both $\sigma_{t\bar{t}}$ and $A_{FB}$, due to normalization and shape uncertainties associated with the dominant backgrounds. Profiting for Ref. [15], where $\hat{\mu}_t$ is shown to be closely related to the quantities mentioned above, we can confidently expect that the uncertainty on the CMDM can also be reduced to a similar level. Specifically, for the $\hat{\mu}_t$ reported in Eq. (1), where the statistical and systematic uncertainties have comparable fractional contributions, a simple analysis assuming a reduction to the statistical uncertainty component to 10% of its current value (conservatively taking the largest reported value, $\sigma_{\text{stat}} = 0.013$) and a systematic uncertainty reduction to 10% of its current value (again conservatively taking the largest value, $\sigma_{\text{sys}} = 0.016$) lead to a total uncertainty of $\sigma_{\text{tot}} = 0.002$ for the CMDM. Thus, provided that such improvements are achieved, which are not unrealistic given the analysis and methodologies mentioned above, the SM BLHM deviations predicted in this work would become experimentally accessible.

At the FCC-hh [83,99], operating at a center-of-mass energy of ∼100 TeV, the direct discovery of new particles is the primary goal, with the BLHM expected to manifest through its rich spectrum; for example, top CMDM measurements selecting ultraboosted $\bar{t}t$ events lead to enhanced contributions as large as of an order of magnitude compared to 14 TeV LHC projections [100]. Nevertheless, direct searches and indirect precision measurements are complementary, as deviations in SM observables can probe physics beyond the collider kinematic reach [83,99]. The top-quark CMDM provides a sensitive indirect probe of the BLHM, particularly in scenarios where only the lightest top partners are directly accessible, while heavier states remain experimentally challenging due to suppressed cross sections and complex final states [101–103]. A deviation of the top CMDM at the level of $\sim 10^{-3}$ would probe physics associated with Higgs naturalness and indirectly the heavy top partner sector. Moreover, since the CMDM is sensitive to the top partner masses, a precise measurement may test the BLHM prediction of minimized top partner masses and distinguish this "bestest" property from other little Higgs models [104,105].

## VII. CONCLUSIONS

In this work, we compute the CMDM of the top quark within the BLHM framework. For the first time, we include contributions from flavor-changing interactions in the BLHM, introduced through an extended CKM matrix. We study the top-quark CMDM across a range of experimentally allowed values of the $\tan\beta$ parameter. Within the allowed BLHM parameter space—constrained by Higgs sector corrections and fine-tuning considerations—we find CMDM values on the order of $10^{-3}$. This represents a significant improvement over previous BLHM results [13], which did not account for flavor-mixing effects.

The CMDM serves as an alternative probe for BSM heavy quarks, particularly given that experimental searches have so far found no evidence for such quarks below 2.3 TeV for $T$ and $B$ [41] and below 1.42 TeV for exotic states such as $T^{5/3}$, $T^{6}$, and $T^{2/3}$ [42]. However, the current experimental precision on $\hat{\mu}_t$ remains limited, with uncertainties as large as 85%. Further improvements in measurement precision are, therefore, necessary for this observable to become competitive with direct searches.

We have thoroughly propagated all sources of uncertainty to obtain robust uncertainty bands in our CMDM predictions. This enables precise assessment of the extent to which deviations arising from experimental uncertainties can be accommodated within the statistical and theoretical uncertainties of the CMDM BLHM.

Finally, the separation observed among our CMDM predictions for the six studied cases—particularly the smaller differences among cases I, III, V, and VI—can be attributed to the specific flavor-changing processes considered in this work. This outcome highlights the potential for future investigations into mixing with other quark generations.

## ACKNOWLEDGMENTS

T. C.-P. thanks Sistema Nacional de Investigadores e Investigadoras (SNII) and Secretaría de Ciencia, México.

## DATA AVAILABILITY

The data that support the findings of this article are not publicly available. The data are available from the authors upon reasonable request.

## APPENDIX: FEYNMAN RULES IN THE BLHM

In this appendix, we present the Feynman rules that involve flavor changing in the BLHM. The rest of the vertices used can be found in [13,22].

Tables V–VII summarize the Feynman rules for the three-point interactions: fermion-fermion-scalar (FFS), fermion-fermion-gauge (FFV), gauge-gauge-gauge (VVV), and scalar-gauge-gauge (SVV) interactions.

TABLE V. Essential Feynman rules in the BLHM for studying the CMDM.

| Vertex | Rule (factors in Tables VI and VII) |
|---|---|
| $W'^{-}\bar{B}t$ | $\frac{-igs_\beta v}{4\sqrt{2}f}A_y\gamma^\mu P_L(V_{Hu})$ |
| $\eta^{-}\bar{B}t$ | $\frac{4im_W^2}{f^2g^2\sqrt{y_1^2+y_2^2(y_1^2+y_3^2)}}(Y_1P_L+Y_2P_R)(V_{Hu})$ |
| $\phi^{-}\bar{B}t$ | $F_aF_b(X_1P_L+X_2P_R)(V_{Hu})$ |
| $H^{-}\bar{B}t$ | $\frac{-3\sqrt{2}m_Wc_\beta s_\beta y_1y_2y_3^2}{fg\sqrt{y_1^2+y_2^2(y_1^2+y_3^2)}}P_L(V_{Hu})$ |

TABLE VI. Factors from Table V.

| Factor | Expression |
|---|---|
| $A_y$ | $y_3(2y_1^2-y_2^2)(y_1^2+y_2^2)^2(y_1^2+y_3^2)$ |
| $Y_1$ | $B_1+B_2$ |
| $Y_2$ | $B_3+B_4$ |
| $F_a$ | $\frac{y_3(2y_1^2-y_2^2)}{(y_1^2+y_3^2)\sqrt{y_1^2+y_2^2}}$ |
| $F_b$ | $\frac{Fs_\beta}{2f\sqrt{2(f^2+F^2)}}$ |
| $X_1$ | $A_1+A_3+A_6$ |
| $X_2$ | $A_2+A_4+A_5$ |

TABLE VII. Factors from Table VI.

| | |
|---|---|
| $B_1$ | $y_1y_2(y_1^2+y_3^2)c_\beta^2$ |
| $B_2$ | $y_1^3y_2s_\beta-\frac{1}{2}y_1y_2y_3^2s_\beta$ |
| $B_3$ | $\frac{fg}{4m_W}y_3(2y_1^2+5y_2^2)\sqrt{y_1^2+y_3^2}s_\beta$ |
| $B_4$ | $-y_1^3y_3s_\beta-\frac{1}{2}y_1(y_2^2+y_3^2)s_\beta$ |
| $A_1$ | $\frac{-4m_Wc_\beta^2y_1y_2(y_1^2+y_3^2)}{s_\beta y_3(2y_1^2-y_2^2)}$ |
| $A_2$ | $fg-y_1^8-m_Ws_\beta y_3y_2^6-3y_2y_1^4(2y_1^2-y_2^2)-y_1^6(3y_2^2+y_3^2)-y_1^2y_2^4(y_2^2+3y_3^2)$ |
| $A_3$ | $\frac{-4m_Wy_1^3y_2y_3}{2y_1^2-y_2^2}$ |
| $A_4$ | $\frac{8m_Wy_1^3(y_2^2+y_3^2)}{2y_1^2-y_2^2}$ |
| $A_5$ | $\frac{-4m_Wy_1^3}{2y_1^2-y_2^2}$ |
| $A_6$ | $\frac{4m_Wy_1^3y_2}{y_3(2y_1^2-y_2^2)}$ |


[1] M. Schmaltz, D. Stolarski, and J. Thaler, J. High Energy Phys. 09 (2010) 018.
[2] R. Martinez, M. A. Perez, and N. Poveda, Eur. Phys. J. C **53**, 221 (2008).
[3] J. I. Aranda, T. Cisneros-Pérez, J. Montaño, B. Quezadas-Vivian, F. Ramírez-Zavaleta, and E. S. Tututi, Eur. Phys. J. Plus **136**, 164 (2021).
[4] R. Martinez and J. A. Rodriguez, Phys. Rev. D **65**, 057301 (2002).
[5] J. I. Aranda, D. Espinosa-Gómez, J. Montaño, B. Quezadas-Vivian, F. Ramírez-Zavaleta, and E. S. Tututi, Phys. Rev. D **98**, 116003 (2018).
[6] J. Montano-Domínguez, F Ramírez-Zavaleta, E. S. Tututi, and E. Urquiza-Trejo, J. Phys. G **50**, 115004 (2023).
[7] L. Ding and C. X. Yue, Commun. Theor. Phys. **50**, 441 (2008).
[8] A. I. Hernández-Juárez, G. Tavares-Velasco, and A. Moyotl, Chin. Phys. C **45**, 113101 (2021).

[9] R. Martinez and J. A. Rodriguez, Phys. Rev. D **55**, 3212 (1997).
[10] A. I. Hernández-Juárez, A. Moyotl, and G. Tavares-Velasco, Phys. Rev. D **98**, 035040 (2018).
[11] R. Martinez, M. A. Perez, and O. A. Sampayo, Int. J. Mod. Phys. A **25**, 1061 (2010).
[12] Subhadip Bisal, Phys. Lett. B **855**, 138848 (2024).
[13] J. I. Aranda, T. Cisneros-Pérez, E. Cruz-Albaro, J. Montaño-Domínguez, and F. Ramírez-Zavaleta, arXiv: 2111.03180.
[14] A. Sirunyan *et al.*, Phys. Rev. D **100**, 072002 (2019).
[15] A. Sirunyan *et al.*, J. High Energy Phys. 06 (2020) 146.
[16] T. Cisneros-Pérez, M. A. Hernández-Ruíz, A. Gutiérrez-Rodríguez, and E. Cruz-Albaro, Eur. Phys. J. C **83**, 1093 (2023).
[17] M. Kobayashi and T. Maskawa, Prog. Theor. Phys. **49**, 652 (1973).
[18] G. Aad, B. Abbott *et al.* (ATLAS Collaboration), J. High Energy Phys. 06 (2021) 145.
[19] G. Aad, E. Aakvaag *et al.* (ATLAS Collaboration), J. High Energy Phys. 08 (2024) 013.
[20] G. Aad *et al.* (ATLAS Collaboration), Phys. Rev. D **101**, 012002 (2020).
[21] E. Cruz-Albaro, A. Gutiérrez-Rodríguez, J. I. Aranda, and F. Ramírez-Zavaleta, Eur. Phys. J. C **82**, 1095 (2022).
[22] E. Cruz-Albaro, A. Gutierrez-Rodrıguez, M. A. Hernandez-Ruız, and T. Cisneros-Perez, Eur. Phys. J. Plus **138**, 506 (2023).
[23] E. Cruz-Albaro and A. Gutiérrez-Rodríguez, Eur. Phys. J. Plus **137**, 1295 (2022).
[24] T. Cisneros-Pérez, E. Cruz-Albaro, A. Ojeda-Castañeda, and S. Solís-Núñez, Chin. Phys. C **48**, 103109 (2024).
[25] K. Moats, 10.22215/etd/2012-09748 (2012).
[26] M. Blanke, A. J. Buras, A. Poschenrieder, S. Recksiegel, C. Tarantino, S. Uhlig, and A. Weiler, Phys. Lett. B **646**, 253 (2007).
[27] M. Blanke, A. J. Buras, A. Poschenrieder, S. Recksiegel, C. Tarantino, S. Uhlig, and A. Weiler, J. High Energy Phys. 01 (2007) 066.
[28] T. A. W. Martin, 10.22215/etd/2012-09697 (2012).
[29] S. Godfrey, T. Gregoire, P. Kalyniak, T. A. W. Martin, and K. Moats, J. High Energy Phys. 04 (2012) 032.
[30] P. Kalyniak, T. Martin, and K. Moats, Phys. Rev. D **91**, 013010 (2015).
[31] S. Rappoccio, Rev. Phys. **4**, 100027 (2019).
[32] G. Aad *et al.* (ATLAS Collaboration), Eur. Phys. J. C **81**, 396 (2021).
[33] G. Aad *et al.* (ATLAS Collaboration), Phys. Lett. B **744**, 163 (2015).
[34] A. M. Sirunyan *et al.* (CMS Collaboration), J. High Energy Phys. 03 (2020) 055.
[35] M. Hashemi and G. Haghighat, Eur. Phys. J. C **79**, 419 (2019).
[36] A. Tumasyan *et al.* (CMS Collaboration), J. High Energy Phys. 09 (2023) 032.
[37] G. Aad *et al.* (ATLAS Collaboration), J. High Energy Phys. 06 (2021) 145.
[38] A. Tumasyan *et al.* (CMS Collaboration), J. High Energy Phys. 09 (2023) 051.
[39] A. Tumasyan *et al.* (CMS Collaboration), Phys. Rev. D **105**, 032008 (2022).
[40] A. M. Sirunyan *et al.* (CMS Collaboration), Eur. Phys. J. C **81**, 688 (2021).
[41] G. Aad *et al.* (ATLAS Collaboration), J. High Energy Phys. 08 (2023) 153.
[42] G. Aad *et al.* (ATLAS Collaboration), Eur. Phys. J. C **83**, 719 (2023).
[43] M. Aaboud *et al.* (ATLAS Collaboration), J. High Energy Phys. 07 (2018) 089.
[44] A. M. Sirunyan *et al.* (CMS Collaboration), J. High Energy Phys. 08 (2018) 177.
[45] J. Hubisz, S. Lee, and G. Paz, J. High Energy Phys. 06 (2006) 041.
[46] M. Blanke, A. Buras, A. Poschenrieder, C. Tarantino, S. Uhlig, and Weiler, J. High Energy Phys. 11 (2006) 003.
[47] V. Shtabovenko, R. Mertig, and F. Orellana, Comput. Phys. Commun. **256**, 107478 (2020).
[48] H. H. Patel, Comput. Phys. Commun. **218**, 66 (2017).
[49] R. L. Workman *et al.* (Particle Data Group Collaboration), Prog. Theor. Exp. Phys. **2022**, 083C01 (2022).
[50] B. Efron and R. J. Tibshirani, *An Introduction to the Bootstrap* (Chapman and Hall, London, 1993).
[51] H. García-Tecocoatzi, A. Giachino, J. Li, A. Ramirez-Morales, and E. Santopinto, Phys. Rev. D **107**, 034031 (2023).
[52] A. M. Sirunyan *et al.* (CMS Collaboration), J. High Energy Phys. 06 (2020) 146.
[53] B. Maier, S. M. Narayanan, G. de Castro, M. Goncharov, C. Paus, and M. Schott, Mach. Learn. Sci. Tech. **3**, 025012 (2022).
[54] A. T. Sugunan *et al.* (CMS Collaboration), Proc. Sci. ICHEP2024 (**2025**) 977.
[55] H. Qu and L. Gouskos, Phys. Rev. D **101**, 056019 (2020).
[56] S. Gong, Q. Meng, J. Zhang, H. Qu, C. Li, S. Qian, W. Du, Z. M. Ma, and T. Y. Liu, J. High Energy Phys. 07 (2022) 030.
[57] V. Mikuni and B. Nachman, Phys. Rev. D **111**, 054015 (2025).
[58] A. Tumasyan *et al.* (CMS Collaboration), Phys. Rev. Lett. **131**, 041803 (2023).
[59] O. Cerri (CMS Collaboration), arXiv:1810.00860; H. García-Tecocoatzi, A. Giachino, J. Li, A. Ramirez-Morales, and E. Santopinto, Phys. Rev. D **107**, 034031 (2023).
[60] O. Brüning, H. Gray, K. Klein, M. Lamont, M. Narain, R. Polifka, and L. Rossi, Rep. Prog. Phys. **85**, 046201 (2022).
[61] C. Botta, G. Cerminara, K. Park, and P. Viscone, EPJ Web Conf. **337**, 01026 (2025).
[62] M. Wiehe (CMS Collaboration), Nucl. Instrum. Methods Phys. Res., Sect. A **1041**, 167312 (2022).
[63] G. Aad *et al.* (ATLAS Collaboration), Mach. Learn. Sci. Tech. **5**, 035051 (2024).
[64] A. Hayrapetyan *et al.* (CMS Collaboration), Eur. Phys. J. C **85**, 495 (2025).
[65] R. D. Ball *et al.* (NNPDF Collaboration), Eur. Phys. J. C **82**, 428 (2022).
[66] R. D. Ball *et al.* (NNPDF Collaboration), Eur. Phys. J. C **84**, 517 (2024).

[67] D. d'Enterria, S. Kluth, G. Zanderighi, C. Ayala, M. A. Benitez-Rathgeb, J. Bluemlein, D. Boito, N. Brambilla, D. Britzger, S. Camarda *et al.*, J. Phys. G **51**, 090501 (2024).
[68] A. Hayrapetyan *et al.* (CMS Collaboration), Eur. Phys. J. C **84**, 26 (2024).
[69] A. Hayrapetyan *et al.* (CMS Collaboration), Phys. Rep. **1115**, 116 (2025).
[70] ATLAS Collaboration, Report No. ATL-PHYS-PUB-2023-029, 2023, https://cds.cern.ch/record/2872787.
[71] CMS Collaboration, Report No. CMS-NOTE-2018-006, 2018, https://cds.cern.ch/record/2650976.
[72] J. de Blas *et al.* CERN Yellow Rep. Monogr. **3**, 1 (2018).
[73] P. Bambade, T. Barklow, T. Behnke, M. Berggren, J. Brau, P. Burrows, D. Denisov, A. Faus-Golfe, B. Foster, K. Fujii *et al.*, arXiv:1903.01629.
[74] D. d'Enterria, *Particle Physics at the Year of Light* (World Scientific, Singapore, 2017).
[75] T. Barklow, J. Brau, K. Fujii, J. Gao, J. List, N. Walker, and K. Yokoya, arXiv:1506.07830.
[76] A. Abada *et al.* Eur. Phys. J. Special Topics **228**, 261 (2019).
[77] X. C. Lou, Nat. Rev. Phys. **1**, 232 (2019).
[78] CEPC Study Group arXiv:1809.00285.
[79] CEPC Study Group Collaboration, arXiv:1811.10545.
[80] Z. Li, X. Sun, Y. Fang, G. Li, S. Xin, S. Wang, Y. Wang, Y. Zhang, H. Zhang, and Z. Liang, Eur. Phys. J. C **83**, 269 (2023); **83**, 501(E) (2023).
[81] X. Ai, S. Antusch, P. Athron, Y. Bai, S. S. Bao, D. Barducci, X. J. Bi, T. Cai, L. Calibbi, J. Cang *et al.*, Chin. Phys. C **49**, 123108 (2025).
[82] The Circular Electron Positron Collider, 10.1038/s42254-019-0047-1.
[83] M. Benedikt *et al.* (FCC Collaboration), Eur. Phys. J. C **85**, 1468 (2025).
[84] T. Behnke, J. E. Brau, B. Foster, J. Fuster, M. Harrison, J. M. Paterson, M. Peskin, M. Stanitzki, N. Walker, and H. Yamamoto, arXiv:1306.6327.
[85] P. N. Burrows *et al.* (CLICdp and CLIC Collaboration), CERN Yellow Rep. Monogr. **2**, 1 (2018).
[86] T. Lastovicka, K. Seidel, and J. Strube, arXiv:1202.6170.
[87] F. Blekman, F. Canelli, A. De Moor, K. Gautam, A. Ilg, A. Macchiolo, and E. Ploerer, Eur. Phys. J. C **85**, 165 (2025).
[88] L. Linssen, A. Miyamoto, M. Stanitzki, and H. Weerts, 10.5170/CERN-2012-003.
[89] A. Drutskoy, *International Linear Collider (ILC)* (Morgan & Claypool Publishers, 2018), 10.1088/2053-2571/aae221.
[90] E. Sicking and R. Ström, Nat. Phys. **16**, 386 (2020).
[91] R. Brenner and C. Leonidopoulos, Eur. Phys. J. Plus **136**, 1198 (2021).
[92] S. Prestel, J. High Energy Phys. 11 (2021) 041.
[93] M. Chiesa, C. L. Del Pio, G. Montagna, O. Nicrosini, F. Piccinini, and F. P. Ucci, Phys. Rev. D **112**, 1 (2025).
[94] J. F. Kamenik, A. Lusiani, S. Monteil, and G. Wilkinson, *European Strategy for Particle Physics Update 2025-2026, Contribution ID 196* (European Strategy Group (ESG), Switzerland, 2025), https://indico.cern.ch/event/1439855/contributions/6461584/.
[95] B. Zhou and J. Gao, J. High Energy Phys. 02 (2025) 003.
[96] A. Juste, S. Mantry, A. Mitov, A. Penin, P. Skands, E. Varnes, M. Vos, and S. Wimpenny, Eur. Phys. J. C **74**, 3119 (2014).
[97] A. Juste, S. Mantry, A. Mitov, A. Penin, P. Skands, E. Varnes, M. Vos, and S. Wimpenny, Eur. Phys. J. C **74**, 3119 (2014).
[98] H. Abramowicz *et al.* (CLICdp Collaboration), J. High Energy Phys. 11 (2019) 003.
[99] M. Benedikt and F. Zimmermann, Nat. Rev. Phys. **1**, 238 (2019).
[100] J. A. Aguilar-Saavedra, B. Fuks, and M. L. Mangano, Phys. Rev. D **91**, 094021 (2015).
[101] D. Barducci, A. Belyaev, M. Buchkremer, G. Cacciapaglia, A. Deandrea, S. De Curtis, J. Marrouche, S. Moretti, and L. Panizzi, J. High Energy Phys. 12 (2014) 080.
[102] X. Y. Tian, L. F. Du, and Y. B. Liu, Eur. Phys. J. C **81**, 594 (2021).
[103] M. Backovic, T. Flacke, J. H. Kim, and S. J. Lee, J. High Energy Phys. 04 (2016) 014.
[104] M. Perelstein, Prog. Part. Nucl. Phys. **58**, 247 (2007).
[105] M. Schmaltz and D. Tucker-Smith, Annu. Rev. Nucl. Part. Sci. **55**, 229 (2005).